Macromolecules

Article

pubs.acs.org/Macromolecules

Thermoset Blends of an Epoxy Resin and Polydicyclopentadiene

Brian J. Rohde, Kim Mai Le, Ramanan Krishnamoorti,* and Megan L. Robertson*

Department of Chemical and Biomolecular Engineering, University of Houston, Houston, Texas 77204-4004, United States

Supporting Information

ABSTRACT: The mechanical properties of two chemically distinct and complementary thermoset polymers were manipulated through development of thermoset blends. The thermoset blend system was composed of an anhydride-cured diglycidyl ether of bisphenol A (DGEBA)-based epoxy resin, contributing high tensile strength and modulus, and polydicyclopentadiene (PDCPD), which has a higher toughness and impact strength as compared to other thermoset polymers. Ultra-small-angle and small-angle X-ray scattering analysis explored the morphology of concurrently cured thermoset blends, revealing a macroscopically phase separated system with a surface fractal structure across blended systems of varying composition. The epoxy resin rich and PDCPD rich phases exhibited distinct glass transitions (T_g's): the T_g observed at higher temperature was associated with the epoxy resin rich phase and was largely unaffected by the presence of PDCPD, whereas the PDCPD rich phase T_g systematically decreased with increasing epoxy resin content due to inhibition of dicyclopentadiene ring-opening metathesis polymerization. The mechanical properties of these phase-separated blends were in reasonable agreement with predictions by the rule of mixtures for the blend tensile strength, modulus, and fracture toughness. Scanning electron microscopy analysis of the tensile and fracture specimen fracture surfaces showed an increase in energy dissipation mechanisms, such as crazing, shear banding, and surface roughness, as the fraction of the more ductile component, PDPCD, increased. These results present a facile method to tune the mechanical properties of a toughened thermoset network, in which the high modulus and tensile strength of the epoxy resin can be largely retained at high epoxy resin content in the blend, while increasing the fracture toughness.

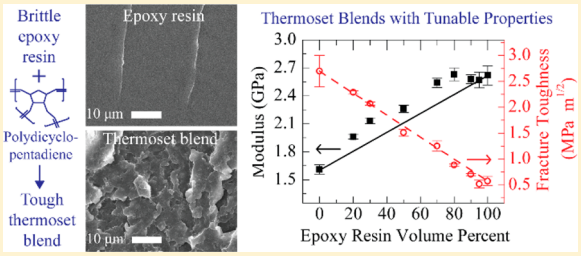

1. INTRODUCTION

Progression into a more environmentally conscious society has led to a strong desire to pursue energy production from renewable and sustainable sources. Offshore wind is a largely underutilized energy source that is becoming increasing popular due to high wind strength and potential for placement of large scale wind farms away from communities.[1,2] The blades of wind turbines are massive structures composed in large part of fiber reinforced epoxy resins, which find use in applications where high strength and low weight are desirable. However, epoxy resins are well established to suffer from brittle failure: the material undergoes catastrophic failure once sufficient stress has been reached to propagate a crack due to the inability to dissipate energy away from crack growth.[3−5] The composites used to construct wind turbine blades are typically composed of around 50 wt % epoxy resin, and improvements to the mechanical properties of the epoxy resin manifest themselves in the ability to build larger structures that can capture more wind energy, operate in stronger wind patterns, and produce more power output per given area.[1,2]

Techniques for toughening epoxy resins often employ additives which promote energy dissipation away from crack growth through processes such as crazing, shear banding, particle bonding, cavitation, crack pinning, and crack diversion.[6−19] Toughening additives include, but are not limited to, rubber particles, carbon black, core−shell particles, and block copolymers.[6−19] While these methods have found success, there are typically decreases in thermal and mechanical properties (such as in the case of rubber toughening) or difficulties in achieving proper dispersion within the epoxy matrix (such as in the case of (nano)particle addition).[8,20,21] Challenges preventing sufficient dispersion are further compounded within the composite as the particulates are unable to transverse regions between the glass fibers to achieve homogeneous concentration throughout the length of the composite due to kinetic or processing limitations.[22]

Polymer blending is an effective strategy to develop new materials which possess beneficial properties, combining desirable attributes of two or more polymers. Blending is often used in industrial applications of polymeric materials as it provides a facile route to tuning properties (mechanical, thermal, etc.) through varying blend composition and does not require the costly synthesis of new polymers to achieve desired physical behavior.[23,24] Blending strategies have traditionally been employed for tuning the properties of thermoplastics, with blend morphology often manipulated through the addition of compatibilizers which reduce the interfacial tension and improve interfacial adhesion.[23−26] By contrast, there are few reports in the literature on the development of thermoset blends in which two thermoset polymers are cured either

Received: July 29, 2016
Revised: September 20, 2016

DOI: 10.1021/acs.macromol.6b01649
Macromolecules XXXX, XXX, XXX−XXX

sequentially or simultaneously. The majority of efforts in producing thermoset blends have emphasized the preparation of interpenetrating polymer networks (IPNs). While true IPNs are homogeneously mixed at the molecular level, disparate curing kinetics and unfavorable interactions between the blend components often give rise to phase-separated systems.[27−31] Lacking in the literature are detailed investigations of controlling such phase-separated thermoset blend morphologies, providing alternative routes to thermosets with tunable properties.

Here, we explore the preparation of thermoset blends containing an anhydride-cured epoxy resin and polydiclopentadiene (PDCPD) cured via ring-opening metathesis polymerization (ROMP). In these thermoset blends, PDCPD contributes toughness, and the epoxy resin contributes high tensile strength and modulus. This work is a departure from prior literature studies in which dicyclopentadiene monomer was encapsulated within an epoxy resin matrix to promote self-healing.[32] In this work, we develop cured thermoset blends of PDCPD and the epoxy resin. We have previously reported the curing kinetics in this thermoset blend system, in which each network is highly influenced by the presence of the other.[33] In this article, we explore structural behavior of epoxy resin/PDCPD blends and their resultant glass transitions and tensile and fracture behavior. Despite the presence of phase-separated microstructures, the facile preparation of these blends provides convenient access to tunability of the thermal and mechanical properties.

2. EXPERIMENTAL METHODS

2.1. Materials. The diglycidyl ether of bisphenol A (DGEBA) was supplied by Dow Chemical in the form of Dow Epoxy Resin (D.E.R.) 331 (the fraction of DGEBA molecules that are prepolymerized and possess an extra hydroxyl-containing midgroup, n, = 0.15). Nadic methyl anhydride (NMA, >95% purity) and dicyclopentadiene (DCPD) with butylated hydroxytoluene as a stabilizer (>96% purity) were purchased from Sigma-Aldrich and used as received. The second-generation Grubbs' catalyst (G2, used in the ring-opening metathesis polymerization of DCPD) was purchased from Sigma-Aldrich and stored under an ultrapure nitrogen environment. An epoxy resin catalyst, 2,4,6-tri(dimethylaminomethyl)phenol, was supplied by Air Products as Ancamine K54 (referred to as K54 in this article) and used as received.

2.2. Blend Nomenclature. Blends are labeled as *xx*E, where *xx* corresponds to the vol % of epoxy resin (consisting of DGEBA, NMA, and K54). The remaining volume corresponds to PDCPD. For example, blend 30E is 30 vol % epoxy resin and 70 vol % PDCPD.

2.3. Preparation and Curing of Epoxy Resin. Pure DGEBA was cured using 95.3 phr (parts per hundred parts by weight of DGEBA resin) of NMA and 1 phr K54. This corresponds to the following concentration of each component: 50.9 wt % of DGEBA, 48.5 wt % of NMA, and 0.6 wt % of K54. Components were mixed using a Cole−Parmer Stir-Pak heavy duty mixer with an impeller blade. A large master batch of the mixture was prepared and used throughout for blends and neat epoxy resin curing. Neat epoxy resin was poured into the tensile and fracture toughness molds and cured for 1 h at 30 °C, 2 h at 70 °C, 5 h at 100 °C, 4 h at 160 °C, and 2 h at 200 °C.

2.4. Preparation and Curing of Neat DCPD. Neat DCPD was melted at 30 °C so that it was easy to work with volumetrically and mix with G2. To make the tensile and fracture specimens, a large volume of DCPD (∼200 mL) was placed under impeller mixing. While the DCPD was under impeller mixing, G2 in an amount corresponding to 5000:1 molar ratio between the DCPD and catalyst was added as received and vigorously mixed. The DCPD and G2 solution was then quickly poured into the tensile and fracture molds (to avoid solidification prior to transfer) and cured for 1 h at 30 °C, 2 h at 70 °C, 5 h at 100 °C, 4 h at 160 °C, and 2 h at 200 °C. Unless otherwise noted, curing was conducted in a convection oven in air. Section 6 of the Supporting Information discusses optimization of the DCPD curing process, including removal of unreacted DCPD monomer. Polymerized DCPD is referred to as PDCPD within this article.

2.5. Preparation and Curing of Epoxy Resin and DCPD Blends. On a 50 mL basis, blends of various volume ratios of the epoxy resin components and DCPD were prepared and mixed using a Cole−Parmer Stir-Pak heavy duty mixer with an impeller blade. When the samples were ready for tensile and fracture toughness molding, G2 was added to the mixture of DCPD and epoxy resin components while the sample was under impeller mixing. The G2 concentration was held constant at 1.5×10^{-3} M. The blends with G2 were vigorously mixed using the impeller mixer and then briefly placed under light vacuum from a diaphragm pump (∼30 s) to remove bubbles induced during mixing. The blends were then poured into the tensile and fracture toughness molds and cured (in a convection oven in air) for 1 h at 30 °C, 2 h at 70 °C, 5 h at 100 °C, 4 h at 160 °C, and 2 h at 200 °C. For samples used in optical microscopy, K54 was omitted from the sample. Optical microscopy slides were prepared by taking a drop of the reactive mixture and sandwiching it between a glass slide and a glass coverslip. The sample was cured overnight at 30 °C to ensure that the polymerization (ROMP) of DCPD had stagnated.

2.6. Optical Microscopy. Optical microscopy was performed on a Leica DM2500 M microscope with a HCX PL FLUOTAR 20×/0.50 BD objective in bright field mode using a mercury lamp. Optical microscopy images were processed using the ImageJ fast Fourier transform (FFT) function. The average domain size (d) was taken to be that at the peak maximum in the intensity versus wavevector ($q = 2\pi/d$) plot. Optical microscopy images were obtained on partially cured blends; the blend preparation procedure is described in section 2.5.

2.7. Differential Scanning Calorimetry. Differential scanning calorimetry (DSC) was performed on a TA Instruments Q2000 DSC calibrated with an indium standard. 10−20 mg was removed from each tensile bar and treated to a heat−cool−heat cycle from 0 to 200 °C at 10 °C/min under 50 mL/min nitrogen flow. For samples with a single T_g, the glass transition temperature (T_g) was taken as the temperature corresponding to 50% of the step change observed during the glass transition from the second heating cycle. For blends 20E, 30E, and 50E, in which two glass transistions were apparent, the derivative heat flow with respect to temperature was corrected for the baseline, and the resulting peak was fit (Voigt profile) to determine the T_g from the peak location (Figures S14−S17). The T_g values determined from the two analysis methods were within 0.5 °C of one another when performed on the single transition of blend 70E.

2.8. Tensile Testing. Tensile testing was carried out at room temperature using an Instron Model 5966 universal tester with a 2 kN load cell at a speed of 10 mm/min. Dogbone-shaped testing bars (following ASTM D638, bar type 5, thickness 3.2 mm) were prepared by pouring unreacted monomer (either neat or blends) in an aluminum mold and following the curing schedule outlined previously. Pneumatic grips (maximum 2 kN) were used to affix the sample in the testing frame, at a compressed air pressure of 90 psi.[34] The measurement was repeated with 20 test specimens for the neat components and 10 test specimens for the blends.

2.9. Fracture Toughness Testing. Fracture toughness specimens were molded following the ASTM D5045 standard and single-edge notched bending geometry (SENB).[35] For the neat epoxy resin and all blends, a bar geometry of 1.225 cm × 0.615 cm × 5.37 cm was used that ensured plane strain criteria was met. For neat PDCPD, a bar geometry of 2.475 cm × 1.190 cm × 10.75 cm was used to accommodate the higher fracture toughness and lower tensile strength when considering plane strain criteria. A Chevron notch was created in each sample using a metal file and then a fresh razor blade, cooled in liquid nitrogen, was gently tapped on the sample to produce a natural crack. Specimens were then tested in a Instron Model 5966 universal tester in compression mode at 10 mm/min under three-point bend geometry. The critical stress intensity factor, K_{IC}, was calculated from

DOI: 10.1021/acs.macromol.6b01649
Macromolecules XXXX, XXX, XXX−XXX

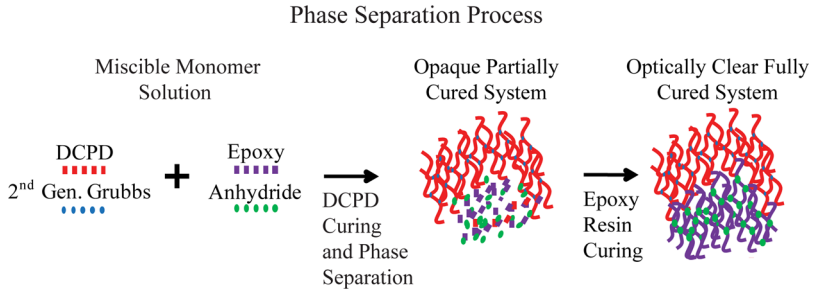

Figure 1. Schematic of the thermoset blend phase separation process. The DCPD and epoxy monomers are miscible with one another but undergo phase separation during the low-temperature curing of DCPD. Once the system is brought to elevated temperatures, the epoxy resin cures within the macroscopically phase-separated blend.

the peak load, P_q, as described in the ASTM D5045 standard. See Supporting Information section 5 for relevant calculations.

2.10. Scanning Electron Microscopy. The fracture surfaces of tensile bars and SENB specimens were imaged using a Jeol JSM-6010LA field emission scanning electron microscope at a voltage of 15 kV. The fracture surface was etched with ionized argon gas and subsequently coated with gold using a Denton Vacuum Desk V sputter coater. The gold thickness was approximately 10 nm.

2.11. Ultra-small-Angle X-ray Scattering and Small-Angle X-ray Scattering. Samples for ultra-small-angle X-ray scattering (USAXS) and small-angle X-ray scattering (SAXS) measurements were prepared following the same mixing and curing schedule described in sections 2.3, 2.4, and 2.5, except that samples were centrifuged for 10 s at 4000 rpm after mixing to remove bubbles and cured in small aluminum pans 1 mm in thickness and 8 mm in diameter. After curing the samples were removed from the pans. USAXS was performed at the Advance Photon Source (APS) at Argonne National Laboratory on beamline 9ID-C, with an energy of 21 keV corresponding to an X-ray wavelength of 0.5904 Å. This instrument employs Bonse−Hart-type double-crystal optics to extend the scattering vector q range down to 0.0001 Å^{-1}. The beam size was approximately 2.0 mm × 1.0 mm. A more detailed description of the instrument can be found in prior publications.[36,37] The data were slit smeared with a slit length of 0.033 069 Å^{-1}. The sample thickness was determined using a micrometer. Instrumental background scattering was determined using an empty cell (no windows were used to encapsulate the sample). USAXS and SAXS data were reduced using the Indra program within Igor, and reduced data were fit using the Guinier−Porod model within the Irena software package for Igor.[38−40]

3. RESULTS AND DISCUSSION

3.1. Investigation of Blend Morphology. Blends of epoxy resin and PDCPD were prepared through a multistage curing protocol in which the DCPD was first cured at low temperature (in two stages at 30 and 70 °C), followed by curing of the epoxy resin at high temperatures (in three stages at 100, 160, and 200 °C). The blends undergo macroscopic phase separation upon curing DCPD in the low temperature stage. At elevated temperatures, the epoxy resin cures within the phase-separated blend (Figure 1). The multistep curing protocol was developed following *in situ* FTIR analysis conducted during curing (neat components and blends) that indicated large disparities in curing kinetics of the neat components.[33] A final postcuring stage of 200 °C was implemented to ensure removal of unreacted DCPD monomer from the specimens (whether neat DCPD or a blend) and drive both reactions to relative completion.

Optical microscopy provides a convenient route to probe the microstructure of the blends following DCPD curing, but prior to curing of the epoxy resin. While the cured PDCPD and epoxy resin exhibited similar refractive indices such that the blend appeared transparent even when macroscopically phase separated, the unreacted epoxy resin components and PDCPD had sufficiently different refractive indices to provide optical contrast for the microscopy experiments. Blends of various volume ratios of DCPD and epoxy resin without K54 catalyst were cured between a microscopy slide and coverslip overnight at 30 °C to allow the PDCPD conversion to stagnate (negligible curing of the epoxy resin occurred under these conditions in the absence of K54 catalyst). Blends across the entire composition range exhibited cocontinuous morphologies, even at low concentrations of DCPD (Figure 2a and Figure S1). By contrast, previous work using a lower G2 concentration showed discrete domains of the minor phase at asymmetric compositions.[33]

Optical micrographs were processed using a fast Fourier transform (FFT) (Figure 2a and Figure S1) and azimuthal averaging (in ImageJ) to produce the intensity as a function of wavevector q, shown in Figure 2b. The average domain size (d_{OM}) was calculated from the q value at the peak in the 1D intensity plot ($d_{OM} = 2\pi/q_{peak}$, Table 1). The resulting domains sizes for all blends were on the order of 2−5 μm, with broad distributions as implied by the peak widths (Figure 2b).[a]

Fully cured epoxy resin/PDCPD blends were examined with USAXS/SAXS, probing structures between 1 and 1000 nm. The absolute scattering intensity as a function of scattering vector q is shown in Figure 3a and Figures S2−S10 for neat components and all blends.

Neat epoxy resin and PDCPD exhibited little scattering intensity with large errors due to overlap with the background (Figure S2) and were not examined further. Data obtained from the blends were analyzed with the generalized Guinier−Porod model with two distinct regions:[39] the Porod region at high-q and an intermediate-q Guinier region:

$$I(q) = \frac{G_1}{q^{s_1}} \exp\left(\frac{q^2 {R_{g1}}^2}{3 - s_1}\right) \quad q \le q_1 \tag{1a}$$

$$I(q) = \frac{D}{q^d} \quad \text{for } q \ge q_1 \tag{1b}$$

where $I(q)$ is the scattering intensity, q is the scattering vector, R_{g1} is the radius of gyration for the intermediate representing the cross-sectional size, d is the Porod exponent, s_1 is the parameter that models nonspherical objects in the intermediate-q region, and G_1 and D represent scaling factors for the intermediate-q Guinier region and high-q Porod region, respectively. The scattering vector q_1 is the crossover q value

DOI: 10.1021/acs.macromol.6b01649
Macromolecules XXXX, XXX, XXX−XXX

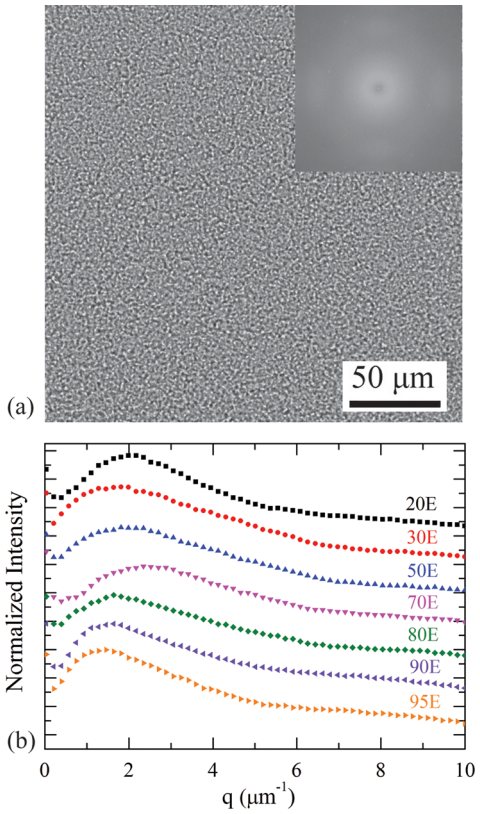

Figure 2. (a) Optical micrograph of blend 50E, cured at 30 °C without the addition of K54 catalyst (under these conditions, PDCPD is cured whereas the epoxy resin is not cured). The inset shows a FFT of the image. The other blends (ranging from 20 to 95 vol % epoxy resin) showed comparable cocontinuous morphologies (Figure S1). (b) Intensity vs wavevector q calculated from the FFT of micrographs of partially cured blends (a representative FFT is shown in the inset to (a)). The domain size, d_{OM}, was calculated from the value of q at the peak maximum. Plots have been shifted along the intensity axis for clarity.

between the Porod region and the intermediate-q Guinier region and is calculated from R_{g1} by

$$q_1 = \frac{1}{R_{g1}}\left[\frac{(d - s_1)(3 - s_1)}{2}\right]^{1/2} \quad (2)$$

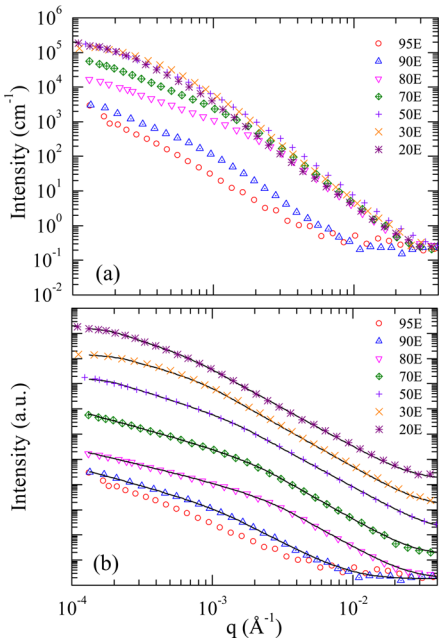

Figure 3. (a) USAXS data (absolute intensity, slit smeared with slit length 0.033 069 Å^{-1}) obtained from epoxy resin/PDCDP blends. Additional data are shown in Figures S2–S10. Every 7th point is shown for clarity. (b) Vertically shifted USAXS data with generalized Guinier–Porod model (eq 1) fit to the high and intermediate q regions, shown as the solid black curves (slit smearing is accounted for in the model fitting). Errors on the intensity measurements are smaller than the size of the symbol and are not shown here (see Figures S2–S10).

The value of the parameter s_1 is indicative of the underlying three-dimensional morphology of the material with s_1 = 0, 1, 2 representing, spherical, rod, and lamellar (or platelet) morphologies, respectively. The model fits to the data are shown in Figure 3b. While some data sets exhibited a turnover from the intermediate-q Guinier region to a low-q Guinier region (blends 50E, 30E, and 20E), the low-q regions contained too few data points to be sufficiently modeled with the Guinier equation. Therefore, in this study only information regarding the cross-sectional area (defined by R_{g1}) and underlying morphology (quantified by s_1) was extracted. The resultant parameter values from the Guinier–Porod fitting are shown in Table 1.

Table 1. Structural and Thermal Properties of Epoxy Resin/PDCPD Blends and Pure Components

sample	epoxy resin (vol %)	d_{OM}[a] (μm)	R_{g1}[b] (nm)	q_1[b] (nm^{-1})	s_1[b]	d[b]	T_g[c] (°C)
epoxy resin	100						148.5 ± 0.5
95E	95	4.5				3.2	158 ± 2
90E	90	4.2	33.7 ± 0.2	0.017	2.5	3.8	150.1 ± 0.6
80E	80	3.7	19.3 ± 0.1	0.041	2.3	4.1	145 ± 3
70E	70	2.8	19.8 ± 0.1	0.033	2.5	4.2	134 ± 3
50E	50	3.2	22.3 ± 0.2	0.024	2.6	4.0	156 ± 6 (123 ± 6)
30E	30	3.5	63.8 ± 0.8	0.014	2.2	4.1	161 ± 3 (142 ± 3)
20E	20	3.1	50.6 ± 1.0	0.011	2.6	4.0	163.8 ± 0.4 (153 ± 2)
PDCPD	0						171 ± 2

[a] d_{OM} is the domain size from optical microscopy. [b] R_{g1}, s_1, q_1, and d are parameters determined from Guinier–Porod fitting to the USAXS data, where R_{g1} is the cross-sectional length, s_1 is the Guinier exponent, q_1 is the q location of the transition from the Guinier to Porod regime (calculated from R_{g1}), and d is the Porod exponent. Errors provided for these parameters are errors from model fitting within Irena. [c] T_g's determined from the DSC second heating ramp. In the case of two distinct T_g's, the transitions were determined using peak locations in the derivative heat flow (Figures S14–S17). The PDCPD rich phase T_g is listed in parentheses. Errors provided for T_g represent bar to bar variation within a sample set.

DOI: 10.1021/acs.macromol.6b01649
Macromolecules XXXX, XXX, XXX–XXX

Blend 95E exhibited Porod scattering with an exponent of 3.2, consistent with a phase-separated structure with rough interfaces. Guinier behavior was not observed in blend 95E in the accessible q-range. As the epoxy resin content was decreased to 20−90 vol %, a clear intermediate-q Guinier region became visible with a slope indicative of a surface fractal type structure beyond lamellae, accompanied by a high-q Porod region with exponent around 4, indicating sharp and smooth interfaces. The corresponding R_{g1} values indicated a decrease in the cross-sectional R_g from 34 nm in blend 90E to around 20 nm in blends 80E and 70E. In blends 50E, 30E, and 20E, a subtle turnover into the low q-region was apparent, representing a decrease in the lateral size to within the accessible q range. Blend 30E exhibited a more pronounced low-q Guinier region, accompanied by an increase in the cross-sectional area (represented by R_{g1}) and diminished intermediate-q region (with a decrease in q_1). Blend 20E exhibited a larger intermediate-q region as R_{g1} decreased once again. These results indicate a surface fractal type structure that decreased in lateral size but increased in width as the composition shifted to higher PDCPD content, until a maximum cross-sectional width was observed for blend 30E, which subsequently decreased for blend 20E.

3.2. Thermal Analysis of Fully Cured Neat Components and Blends. Thermal properties of fully cured neat components (epoxy resin, PDCPD) and blends, prepared for tensile testing, were investigated by DSC. T_g as a function of blend composition is shown in Figure 4 (and tabulated in Table 1). Neat epoxy resin and PDCPD exhibited single T_g's at 148 and 171 °C, respectively. For blends containing 20−50 vol % epoxy resin, two T_g's were readily apparent. The higher transition temperature was attributed to the epoxy resin rich phase, and the lower transition temperature was attributed to the PDCPD rich phase, assigned using the measured neat component heat capacity step changes and known blend compositions.[b] The T_g of the epoxy resin rich phase was relatively constant with blend composition (indicating a lack of plasticization) and consistent with the neat epoxy resin T_g, whereas the T_g of the PDCPD rich phase drastically decreased with decreasing PDCPD content in the blend. The decrease in the T_g of the PDCPD rich phase is likely due to inhibition of the ROMP of DCPD in the presence of the epoxy resin components (thus decreasing conversion), which was previously observed using *in situ* FTIR.[33]

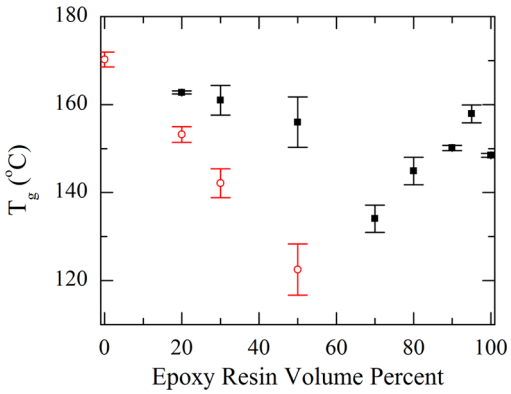

Figure 4. T_g of the neat components and blends, measured on specimens prepared for tensile testing. The open red circles (○) are attributed to the T_g values of the PDCPD rich phase, and the solid squares (■) are attributed to the T_g values of the epoxy resin rich phase. The error bars represent bar to bar variation.

As the epoxy resin content in the blend increased to 70−95 vol %, two key behaviors are observed: only one T_g is present, and the T_g increases as the epoxy resin vol % increases. Blend miscibility is an unlikely explanation for the presence of a single T_g, as USAXS and optical miscopy data indicated strongly phase separated systems (Figures 2 and 3). We hypothesize that low conversion of the PDCPD (based on previous FTIR studies[33]) has reduced the heat capacity step change of the PDCPD rich phase in these blends, thus preventing observation of this transition.[c] The single T_g observed is therefore attributed to the epoxy resin rich phase. Interestingly, the T_g of blend 95E increased slightly relative to the neat epoxy resin, consistent with an increase in conversion due to dilution of epoxy resin with unreacted DCPD monomer[33] (i.e., delaying vitrification).

We now discuss the trend of increasing T_g with increasing epoxy resin content in blends containing 70−95 vol % epoxy resin. A previous study employing *in situ* FTIR indicated an increase in the epoxy resin conversion in the epoxy resin/PDCPD blends relative to the neat epoxy resin, which was relatively insensitive to the PDCPD content in the blend;[33] ATR-FTIR experiments on fully cured tensile bars showed the same behavior (section 7 of the Supporting Information). We therefore do not attribute the depressed T_g in these blends to lower conversion of the epoxy resin. We propose that in blends 70E and 80E drastic inhibition of ROMP of DCPD (and resulting low conversion) may have promoted enhanced miscibility of the PDCPD and epoxy resin rich phases at early stages in the curing process due to the presence of the DCPD monomer. Though structural analysis indicates highly phase-separated blends after the curing was complete, the epoxy resin phase may include a higher PDCPD content, reducing the T_g. We note that there should be negligible monomer content at the end of the curing schedule, due to the high temperature used in the final curing stages (160 °C for 4 h and 200 °C for 2 h, high enough to volatilize any unreacted DCPD monomer).

The cumulative results of optical microscopy, USAXS, thermal analysis, and FTIR (including prior studies[33]) indicate that the blended system is composed of two strongly phase-separated domains: a PDCPD rich phase whose conversion was significantly inhibited by the presence of the epoxy resin components (thus drastically reducing its T_g) and an epoxy resin rich phase which maintained high overall conversion and T_g. A diagram of the proposed morphology, consistent with the USAXS and optical microscopy analyses, is shown in Figure 5.

3.3. Mechanical Properties of Fully Cured Neat Components and Blends. Tensile properties and fracture toughness were measured for neat components and fully cured blends; the results are tabulated in Table 2 and shown in Figure 6. In this thermoset blend system, the epoxy resin was employed to provide high strength and stiffness to the resulting blends. As anticipated, the neat epoxy resin possessed high tensile strength and modulus values (91 MPa and 2.6 GPa, respectively), consistent with prior literature.[22,41] Neat PDCPD exhibited lower tensile strength and modulus as compared to the epoxy resin (53 MPa and 1.61 GPa, respectively).

PDCPD was blended with the epoxy resin to provide ductility and enhanced toughness to the thermoset blend, relative to the neat epoxy resin. The fracture toughness of PDCPD (2.7 MPa $m^{1/2}$) was greater than that of the neat epoxy resin (0.58 MPa $m^{1/2}$) by a factor of around 4−5.

DOI: 10.1021/acs.macromol.6b01649
Macromolecules XXXX, XXX, XXX−XXX

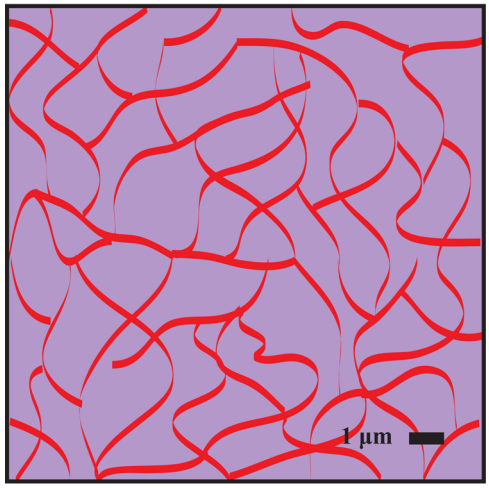

Figure 5. Schematic of the proposed morphology of epoxy resin/PDCPD blends, consistent with USAXS and optical microscopy analyses.

Surprisingly, the elongation at break of PDCPD (7.9%) was only marginally greater than that of the epoxy resin (5.1%), which is in contrast to literature studies which reported large elongation at break values (sometimes greater than 100% elongation).[42−45] We believe this difference is due to the removal of the unreacted DCPD monomer in our specimens, which may have been present when varying curing protocols were used in other studies. To provide evidence for this hypothesis, we explored the mechanical behavior of neat PDCPD under various curing protocols (Figure S24). When the elevated temperature step (200 °C) was eliminated, the resulting mechanical tests showed elongation at break values greater than 100% (Figure S24), attributed to plasticization by the remaining DCPD monomer. By contrast, addition of the 200 °C curing stage (for specimens cured both under vacuum and in air) reduced to the elongation at break values to that reported in Table 2, which are consistent with a prior literature report by Jeong and Kessler, who also used a high postcuring step (at 170 °C).[46]

Modulus and tensile strength values for the blends (Figure 6a) were consistent with or greater than the linear rule of mixtures,[d] indicated by the solid and dashed lines in Figure 6. While the improvement of mechanical properties above the rule of mixtures is often indicative of miscible blends in which the two components are molecularly mixed, creating a material of higher density than the neat components,[47] all other indications as discussed above are that the epoxy resin/PDCPD blends were strongly phase separated. The observed positive deviation from the rule of mixtures is possibly due to ROMP inhibition in the presence of the epoxy resin components, by which the DCPD conversion decreased as the epoxy resin content in the blend increased.[33] The effective epoxy resin content in the blends therefore might be higher than anticipated from the monomer composition, providing better agreement with predictions of the rule of mixtures.

The elongation at break and tensile toughness, however, exhibited negative deviations away from the expected behavior of the rule of mixtures (Figure 6b). The elongation at break of all blends was relatively constant and consistent with that of the neat epoxy resin, regardless of the blend composition. Neat PDCPD exhibited a slightly larger elongation at break than the neat epoxy resin and blends. The tensile toughness values of the neat components were similar to one another, and hence little impact was observed of the blend composition on the tensile toughness (Figure 6b). A slight negative deviation away from the rule of mixtures in the tensile toughness is observed, as the blend tensile toughness values decreased below both neat component values at intermediate epoxy resin vol %. The observed negative deviation of the elongation at break and tensile toughness from the rule of mixtures is most likely due to the blend's rapidly decreasing tensile strength with higher PDCPD content and inability to undergo macroscopic necking/plastic deformation due to rigid epoxy rich domains that extend throughout the material.

Significant differences in the fracture toughness (K_{IC}) values of PDCPD and the epoxy resin led to a strong composition dependence of the fracture toughness on the epoxy resin vol % in the blend, which very closely followed the rule of mixtures (Figure 6c). The radius of the crack tip plastic zone, r_y, was calculated assuming linear-elastic fracture mechanics (under plane strain) as a function of the critical stress intensity value (K_{IC}) and the yield strength (σ_y) (the yield strength and tensile strength were equivalent for the blends reported in Table 2):[22]

$$r_y = \frac{1}{6\pi}\left(\frac{K_{IC}}{\sigma_y}\right)^2 \tag{3}$$

The resultant crack tip plastic zone radii are reported in Table 2. In all blends, the size of the plastic zone at the crack front was as large as or larger than the domain size (Table 1). As the crack front therefore interacted with a representative volume of

Table 2. Mechanical Properties of Blends and Neat Components[a]

sample	tensile strength (MPa)	elongation at break (%)	modulus (GPa)	tensile toughness (MPa)	K_{IC} (MPa m$^{1/2}$)	crack tip radius[b] (μm)
epoxy resin	91 ± 8	5.1 ± 0.8	2.6 ± 0.1	2.7 ± 0.7	0.58 ± 0.09	2.2 ± 1.1
95E	92 ± 8	5.2 ± 0.3	2.57 ± 0.08	2.7 ± 0.3	0.52 ± 0.07	1.7 ± 0.9
90E	100 ± 4	5.8 ± 0.4	2.58 ± 0.05	3.4 ± 0.4	0.70 ± 0.02	2.6 ± 0.4
80E	92 ± 3	5.6 ± 0.5	2.63 ± 0.07	3.1 ± 0.5	0.89 ± 0.02	5.0 ± 0.5
70E	79 ± 2	5.1 ± 0.4	2.54 ± 0.05	2.5 ± 0.3	1.3 ± 0.1	14.4 ± 3.2
50E	75.6 ± 0.8	5.2 ± 0.2	2.26 ± 0.04	2.4 ± 0.2	1.51 ± 0.07	21.2 ± 2.6
30E	73 ± 1	5.6 ± 0.2	2.13 ± 0.03	2.5 ± 0.1	2.07 ± 0.03	42.7 ± 2.4
20E	66 ± 1	5.7 ± 0.6	1.96 ± 0.02	2.4 ± 0.4	2.29 ± 0.03	64 ± 4
PDCPD	53 ± 1	7.9 ± 0.7	1.61 ± 0.05	3.0 ± 0.3	2.7 ± 0.3	138 ± 27

[a]Twenty samples were tested for the neat tensile specimens, 10 samples were tested for the blended tensile specimens, and a minimum of 3 samples (in accordance to ASTM standard 5045) were tested for all SENB specimens. Error bars represent bar to bar variation within a sample set. [b]Calculated with eq 3.

DOI: 10.1021/acs.macromol.6b01649
Macromolecules XXXX, XXX, XXX−XXX

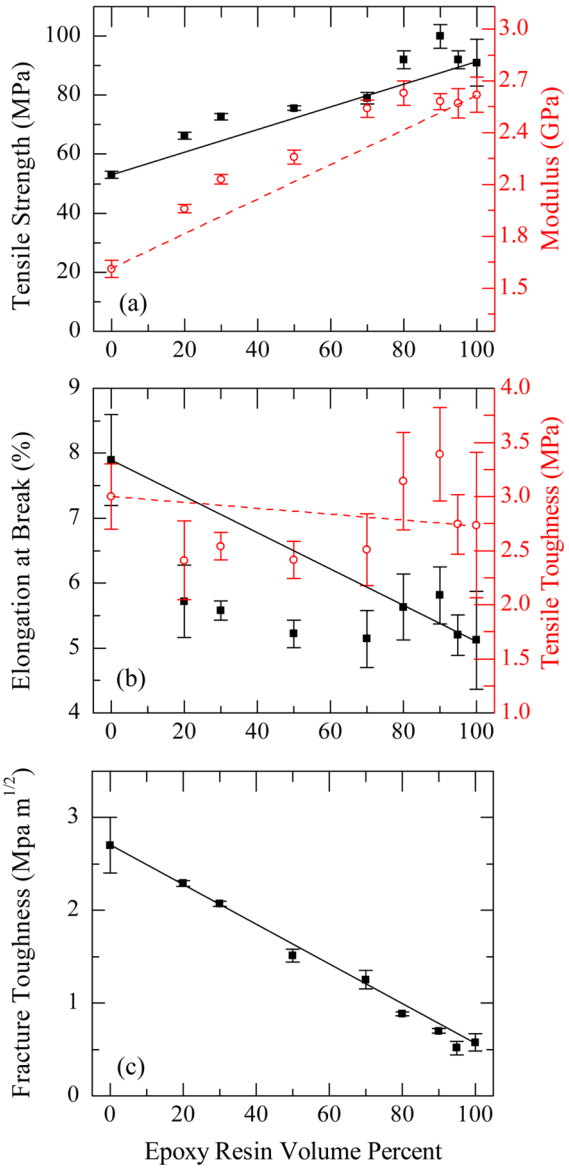

Figure 6. (a) Tensile strength (■) and modulus (red ○) versus blend composition. (b) Elongation at break (■) and tensile toughness (red ○) versus blend composition. (c) Fracture toughness (■) versus blend composition. In all plots, the lines are the linear rule of mixtures calculated from the neat component properties (solid lines are associated with closed data points, and dashed lines are associated with open data points). Error bars represent bar to bar variation within a sample set.

sample, containing both PDCPD rich and epoxy resin rich domains, the resultant blend fracture toughness values followed the rule of mixtures (Figure 6c). Notably, at high epoxy resin content (around 70−90 vol %), the high modulus and tensile strength of the epoxy resin were largely retained while increasing the fracture toughness (Figure 6).

3.4. Investigation of Fracture Mechanisms. The fracture surfaces of tensile and fracture toughness testing specimens were examined with SEM (Figure 7 and Figures S18−S21). The fractographs of both tensile and SENB specimens of all blends exhibited no distinguishable domains (PDCPD or epoxy resin), likely due to lack of mechanical contrast between the phases, and as a result no comparisons to USAXS morphological information could be drawn.

The neat epoxy resin and blends containing 70−95 vol % epoxy resin exhibited behavior consistent with brittle glassy polymers undergoing brittle overload failure.[48−57] In brittle polymers under tension, the material fails by nucleation and cavitation at small defect sites within the bar which propagates outward, creating a relatively smooth surface (mirror) near the defect as the crack propagation is initially relatively slow. As the crack moves outward the speed of the crack front increases and occasional striation/rib structures appear (in the "mist" region) as the secondary crack or cavitation fronts occur and intersect with the initial crack front.[58] Past the mist region the crack rapidly progresses and creates the "hackle" region, in which the failure is critically unstable and the crack is propagating at the highest rate. The sizes of these respective regions and their topologies result from complicated interplay between the yield stress, elastic and shear modulus, and fracture toughness of the material, the size of the defect, the load on the sample, rate of elongation, and the geometry of the bar.[59−61] The tensile bar fracture surfaces showed a qualitative increase in the occurrence of common energy dissipation mechanisms such crazing (fibrils protruding from the crack front) and shear banding (striations perpendicular to the crack edge) as the vol % of PDCPD was increased.[6,8,22,62−64]

In blends containing less than 70 vol % epoxy resin, the tensile specimens no longer failed at a defect and resembled ductile overload failure, in which the intrinsic yield stress of the material is reached before the Griffith criteria describing the onset of brittle failure is satisfied.[54,59] This change in failure mechanism is attributed to the decrease in tensile strength and increase in fracture toughness as the epoxy resin vol % decreased (Figure 6). Tensile specimens for neat PDCPD, shown in Figure S21, underwent shear yielding or "necking", indicative of a ductile material, and had a relatively smooth fracture surface.[65]

In the SENB specimens, a crack was initiated across the sample and plane strain criteria were met. The neat epoxy resin and blend 95E exhibited SENB fracture surfaces which were smoother than their tensile counterparts (as the crack front is standardized in the SENB samples), showing only a few "rivers" that run parallel to the crack front. As a result, nearly no energy was dissipated away from crack growth as indicated by the low fracture toughness of the neat epoxy resin and blend 95E. Additional energy dissipation mechanisms were observed in blends with higher PDCPD content. In blend 90E, the number of striations in the direction of the crack front (typically assigned to out-of-plane deformation/crack growth[48,55]) was significantly increased. Fracture surfaces of blend 70E showed the development of tortuous surfaces that became even more prominent in blend 50E. Such tortuous surfaces allow for greater energy dissipation through the development of new surfaces and are common in tougher samples.[54,59,66] The observation of increased dissipation mechanisms evident in the SEM images of SENB surfaces was in good agreement with the increased fracture toughness of the blends. Blend 20E showed behavior characteristic of microductility, such as fibrils extending from conical features.[48] The neat PDCPD SENB specimen, shown in Figure S21, exhibited textbook hackle markings associated with semibrittle materials containing out-of-plane cracks intersecting with the initial crack front.[48]

4. CONCLUSIONS

The morphological, thermal, and mechanical behavior of epoxy resin/PDCPD blends and their neat components were

DOI: 10.1021/acs.macromol.6b01649
Macromolecules XXXX, XXX, XXX−XXX

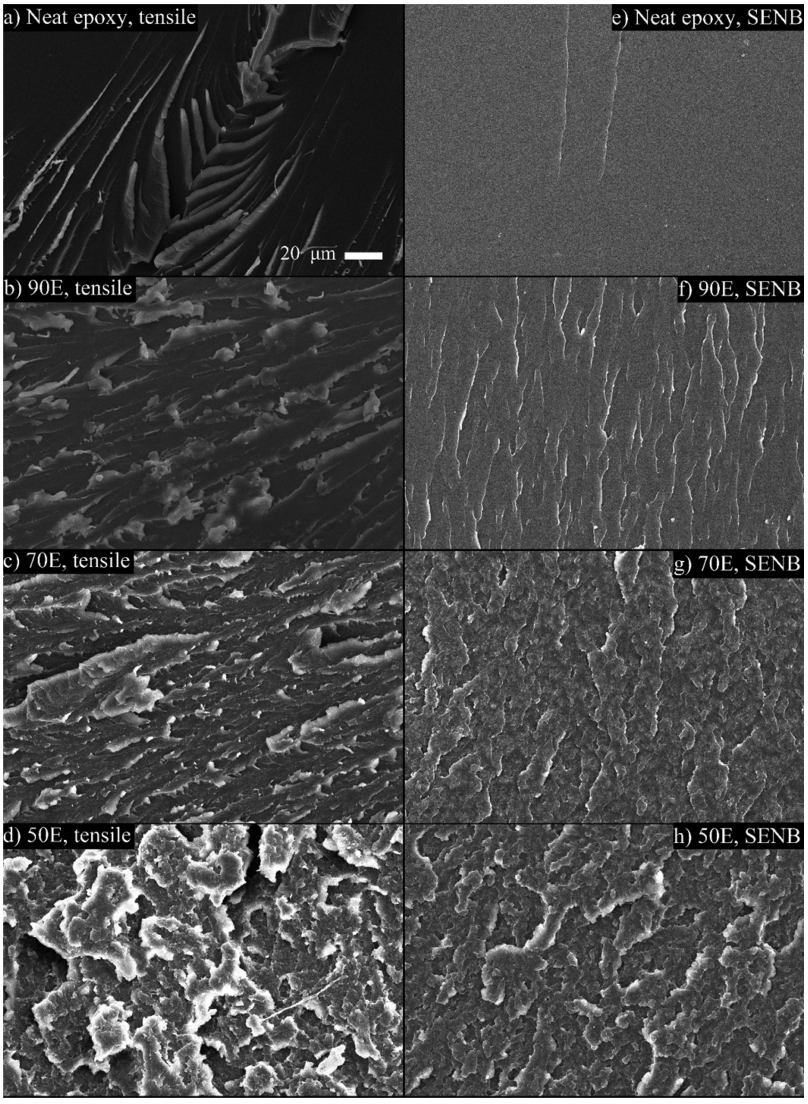

Figure 7. SEM micrographs of the fracture surfaces of tensile specimens (a) neat epoxy resin, (b) 90E, (c) 70E, and (d) 50E and SENB specimens (e) neat epoxy resin, (f) 90E, (g) 70E, and (h) 50E. Additional micrographs of fracture surfaces are provided in Figures S18−S21.

explored. Optical microscopy of partially cured blends indicated cocontinuous phase-separated structures with a common domain size of 2−5 μm across all blend compositions. USAXS analysis of fully cured blends revealed strongly phase-separated systems in the Porod region. Guinier analysis indicated a surface fractal structure for all blends, with cross-sectional length in the range of 20−60 nm and lateral size greater than 2 μm. Two T_g's were observed in blends with 20−50 vol % epoxy resin, characteristic of phase separation. The presence of a single T_g in blends with higher epoxy resin content was attributed to the inability to detect the step change of the PDCPD transition in the DSC measurement (due to lower PDCPD conversion). At low epoxy resin content (20−50 vol %), the T_g of the epoxy resin rich phase was consistent with the neat epoxy resin, and the T_g of the PDCPD rich phase drastically decreased with increasing epoxy resin content due to inhibition of the ROMP reaction. At high epoxy resin content (70−95%), the observed single T_g, associated with the epoxy resin phase systematically increased with increasing epoxy resin content. The depression of the T_g in blends 70E and 80E relative to the neat epoxy resin is proposed to originate with enhanced PDCPD content in the cured epoxy resin phase, mediated by the presence of the DCPD monomer during the blend curing. Neat epoxy resin exhibited a high tensile strength and modulus and behavior typical of brittle specimens, with low fracture toughness. Neat PDCPD exhibited a lower tensile strength and modulus as compared to the epoxy resin; however, the PDCPD fracture toughness was 4−5 times higher than that of neat epoxy resin. Blended systems generally exhibited moduli, tensile strengths, and fracture toughnesses consistent with that predicted by the rule of mixtures. Tensile and fracture testing bars composed of neat epoxy resin and blends containing 70−95 vol % epoxy resin exhibited brittle overload failure. In blends containing less than 70 vol % epoxy resin, the tensile bars exhibited ductile failure and did not appear to fail a defect. Energy dissipation mechanisms such as crazing, shear banding, and surface roughness visually increased with increasing PDCPD content in the blends. These results present a facile method to tune the mechanical properties of a toughened thermoset network, in which the high modulus and tensile strength of the epoxy resin can be largely retained while increasing the fracture toughness.

DOI: 10.1021/acs.macromol.6b01649
Macromolecules XXXX, XXX, XXX−XXX

■ ASSOCIATED CONTENT

Supporting Information

The Supporting Information is available free of charge on the ACS Publications website at DOI: 10.1021/acs.macromol.6b01649.

Raw optical microscopy images of partially cured neat components and blends (Figures S1); USAXS data from cured blends (reduced to absolute scale) (Figures S2−S10); DSC data from cured blends (Figures S11−S17); scanning electron micrographs of tensile and SENB fracture surfaces (Figures S18−S21); critical stress intensity calculations for determination of fracture toughness (eqs S1−S2, Figure S22, Table S1); optimization of neat PDCPD curing schedule (Figures S23−S24); and ATR-FTIR data from cured blends (eq S3, Figure S25, Table S2) (PDF)

■ AUTHOR INFORMATION

Corresponding Authors

*(R.K.) E-mail ramanan@uh.edu, Ph 713-743-4307.

*(M.L.R.) E-mail mlrobertson@uh.edu; Ph 713-743-2748.

Notes

The authors declare no competing financial interest.

■ ACKNOWLEDGMENTS

The authors thank Jeffrey D. Rimer for access to optical microscopy, the University of Houston Department of Civil and Environmental Engineering for SEM access, Charisma Lattao for SEM training, and Mina Dawood and Meng Liu for insightful discussions concerning fracture mechanics and mechanical testing. We are grateful for the assistance of Bin Zhang, whose undergraduate research progressed the mechanical testing for this paper. We appreciate access to Sector 9 at the Advanced Photon Source for USAXS measurements and gratefully acknowledge the contribution of Jan Ilavsky for assistance with USAXS data acquisition and analysis methods. This research used resources of the Advanced Photon Source, a U.S. Department of Energy (DOE) Office of Science User Facility operated for the DOE Office of Science by Argonne National Laboratory under Contract DE-AC02-06CH11357. Data were collected on the USAXS instrument located at 9ID beamline of the APS, operated by X-ray Science Division (XSD). We thank Katrina I. S. Mongcopa and Wenyue Ding for assistance with USAXS experiments. M.L.R., B.J.R., and K.M.L. gratefully acknowledge financial support from the National Science Foundation (Award CMMI-1334838) and the Norman Hackerman Advanced Research Program (Award #003652-0022-2013). This material is based in part upon work supported by the Texas Space Grant Consortium (Contract NNX10AI96H prime award, UTA12-000868 subaward, acknowledged by M.L.R., B.J.R., and K.M.L.). B.J.R. acknowledges support through the National Science Foundation GK-12 Program at the University of Houston (Award DGE-0840889).

■ ADDITIONAL NOTES

[a]We note that surface interactions with the slide and coverslip may perturb the blend morphology observed in optical microscopy, and those effects are neglected here.

[b]Neat PDPCP and epoxy resin exhibited heat capacity step changes of 0.197 and 0.294 J/(g °C), respectively. By comparing the sizes of the peaks in the derivative heat flow of the blends, the T_g's were assigned to either the PDCPD rich phase or the epoxy rich resin phase. For example, in blend 50E the minor peak was attributed to the PDCPD rich phase as the neat PDCPD exhibited a smaller peak in the derivative heat flow compared to the neat epoxy resin. Similarly, in blends 30E and 20E, the larger peak was assigned to the PDCPD rich phase, as PDCPD was expected to be present at higher content [e.g., the anticipated heat capacity step change for the PDCPD rich phase in blend 30E (0.7 × 0.197 J/(g °C)) is greater than the anticipated heat capacity step change for the epoxy resin rich phase (0.3 × 0.294 J/(g °C)].

[c]Figure 4 shows the results of the second heating ramp, in which a lower temperature transition was not observed for blends with 70−95 vol % epoxy resin. However, in the first heating ramp (shown in Figure S13), lower temperature transitions were observed around 80 and 70 °C respectively for blends 70E and 80E.

[d]In the linear rule of mixtures, a straight line is fit to the values measured for neat epoxy resin and neat PDCPD.

■ REFERENCES

(1) Hayman, B.; Wedel-Heinen, J.; Brøndsted, P. Materials Challenges in Present and Future Wind Energy. *MRS Bull.* **2008**, *33* (04), 343−353.

(2) NREL. Large-Scale Offshore Wind Power in the United States, 2010.

(3) Brøndsted, P.; Lilholt, H.; Lystrup, A. Composite Materials for Wind Power Turbine Blades. *Annu. Rev. Mater. Res.* **2005**, *35* (1), 505−538.

(4) Mandell, J. F.; Samborsky, D. D.; Wang, L.; Wahl, N. K. New Fatigue Data for Wind Turbine Blade Materials. *J. Sol. Energy Eng.* **2003**, *125* (4), 506−514.

(5) Samborsky, D. D.; Wilson, T. J.; Mandell, J. F. Comparison of Tensile Fatigue Resistance and Constant Life Diagrams for Several Potential Wind Turbine Blade Laminates. *J. Sol. Energy Eng.* **2009**, *131* (1), 011006−011006.

(6) Sultan, J. N.; McGarry, F. J. Effect of Rubber Particle Size on Deformation Mechanisms in Glassy Epoxy. *Polym. Eng. Sci.* **1973**, *13* (1), 29−34.

(7) Nakamura, Y.; Yamaguchi, M.; Kitayama, A.; Okubo, M.; Matsumoto, T. Effect of particle size on fracture toughness of epoxy resin filled with angular-shaped silica. *Polymer* **1991**, *32* (12), 2221−2229.

(8) Kim, D. S.; Cho, K.; Kim, J. K.; Park, C. E. Effects of Particle Size and Rubber Content on Fracture Toughness in Rubber-modified Epoxies. *Polym. Eng. Sci.* **1996**, *36* (6), 755−768.

(9) Singh, R. P.; Zhang, M.; Chan, D. Toughening of a brittle thermosetting polymer: Effects of reinforcement particle size and volume fraction. *J. Mater. Sci.* **2002**, *37* (4), 781−788.

(10) Varley, R. J. Toughening of epoxy resin systems using low-viscosity additives. *Polym. Int.* **2004**, *53* (1), 78−84.

(11) Paul, D. R.; Robeson, L. M. Polymer nanotechnology: Nanocomposites. *Polymer* **2008**, *49* (15), 3187−3204.

(12) Fu, S.-Y.; Feng, X.-Q.; Lauke, B.; Mai, Y.-W. Effects of particle size, particle/matrix interface adhesion and particle loading on mechanical properties of particulate−polymer composites. *Composites, Part B* **2008**, *39* (6), 933−961.

(13) Liu, J.; Sue, H.-J.; Thompson, Z. J.; Bates, F. S.; Dettloff, M.; Jacob, G.; Verghese, N.; Pham, H. Strain Rate Effect on Toughening of Nano-sized PEP−PEO Block Copolymer Modified Epoxy. *Acta Mater.* **2009**, *57* (9), 2691−2701.

(14) Liu, J.; Sue, H.-J.; Thompson, Z. J.; Bates, F. S.; Dettloff, M.; Jacob, G.; Verghese, N.; Pham, H. Effect of Crosslink Density on Fracture Behavior of Model Epoxies Containing Block Copolymer Nanoparticles. *Polymer* **2009**, *50* (19), 4683−4689.

DOI: 10.1021/acs.macromol.6b01649
Macromolecules XXXX, XXX, XXX−XXX

(15) Liang, Y. L.; Pearson, R. A. The toughening mechanism in hybrid epoxy-silica-rubber nanocomposites (HESRNs). *Polymer* **2010**, *51* (21), 4880−4890.
(16) Salinas-Ruiz, M.; Skordos, A.; Partridge, I. Rubber-toughened epoxy loaded with carbon nanotubes: structure−property relationships. *J. Mater. Sci.* **2010**, *45* (10), 2633−2639.
(17) Giannakopoulos, G.; Masania, K.; Taylor, A. Toughening of epoxy using core−shell particles. *J. Mater. Sci.* **2011**, *46* (2), 327−338.
(18) Krishnamoorti, R.; Vaia, R. A. Polymer nanocomposites. *J. Polym. Sci., Part B: Polym. Phys.* **2007**, *45* (24), 3252−3256.
(19) Kumar, S. K.; Krishnamoorti, R. Nanocomposites: Structure, Phase Behavior, and Properties. *Annu. Rev. Chem. Biomol. Eng.* **2010**, *1* (1), 37−58.
(20) Bergstrom, J. S.; Boyce, M. C. Mechanical Behavior of Particle Filled Elastomers. *Rubber Chem. Technol.* **1999**, *72* (4), 633.
(21) Sheng, N.; Boyce, M. C.; Parks, D. M.; Rutledge, G. C.; Abes, J. I.; Cohen, R. E. Multiscale Micromechanical Modeling of Polymer/Clay Nanocomposites and the Effective Clay Particle. *Polymer* **2004**, *45* (2), 487−506.
(22) Johnsen, B. B.; Kinloch, A. J.; Mohammed, R. D.; Taylor, A. C.; Sprenger, S. Toughening mechanisms of nanoparticle-modified epoxy polymers. *Polymer* **2007**, *48* (2), 530−541.
(23) Koning, C.; Van Duin, M.; Pagnoulle, C.; Jerome, R. Strategies for compatibilization of polymer blends. *Prog. Polym. Sci.* **1998**, *23* (4), 707−757.
(24) Utracki, L. A. Compatibilization of Polymer Blends. *Can. J. Chem. Eng.* **2002**, *80* (6), 1008−1016.
(25) Leibler, L. Block copolymers at interfaces. *Phys. A* **1991**, *172* (1−2), 258−268.
(26) Chen, C. C.; White, J. L. Compatibilizing agents in polymer blends: Interfacial tension, phase morphology, and mechanical properties. *Polym. Eng. Sci.* **1993**, *33* (14), 923−930.
(27) Sperling, L. H.; Mishra, V. The Current Status of Interpenetrating Polymer Networks. *Polym. Adv. Technol.* **1996**, *7* (4), 197−208.
(28) Zhang, Y.; Hourston, D. J. Rigid interpenetrating polymer network foams prepared from a rosin-based polyurethane and an epoxy resin. *J. Appl. Polym. Sci.* **1998**, *69* (2), 271−281.
(29) Raymond, M. P.; Bui, V. T. Epoxy/Castor Oil Graft Interpenetrating Polymer Networks. *J. Appl. Polym. Sci.* **1998**, *70* (9), 1649−1659.
(30) Yeo, J. K.; Sperling, L. H.; Thomas, D. A. Theoretical prediction of domain sizes in IPN's and related materials. *Polymer* **1983**, *24* (3), 307−313.
(31) Lipatov, Y. S.; Alekseeva, T. T. Phase-Separated Interpenetrating Polymer Networks. In *Phase-Separated Interpenetrating Polymer Networks*; Springer: Berlin, 2007; Vol. *208*, pp 1−227.
(32) Kessler, M. R.; Sottos, N. R.; White, S. R. Self-healing structural composite materials. *Composites, Part A* **2003**, *34* (8), 743−753.
(33) Rohde, B. J.; Robertson, M. L.; Krishnamoorti, R. Concurrent curing kinetics of an anhydride-cured epoxy resin and polydicyclopentadiene. *Polymer* **2015**, *69*, 204−214.
(34) Standard Test Method for Tensile Properties of Plastics, ASTM International, 2014.
(35) Committee, D. Test Methods for Plane-Strain Fracture Toughness and Strain Energy Release Rate of Plastic Materials; ASTM International, 2007.
(36) Ilavsky, J.; Jemian, P. R.; Allen, A. J.; Zhang, F.; Levine, L. E.; Long, G. G. Ultra-small-angle X-ray scattering at the Advanced Photon Source. *J. Appl. Crystallogr.* **2009**, *42* (3), 469−479.
(37) Ilavsky, J.; Zhang, F.; Allen, A. J.; Levine, L. E.; Jemian, P. R.; Long, G. G. Ultra-Small-Angle X-ray Scattering Instrument at the Advanced Photon Source: History, Recent Development, and Current Status. *Metall. Mater. Trans. A* **2013**, *44* (1), 68−76.
(38) Long, G. G.; Jemian, P. R.; Weertman, J. R.; Black, D. R.; Burdette, H. E.; Spal, R. High-resolution small-angle X-ray scattering camera for anomalous scattering. *J. Appl. Crystallogr.* **1991**, *24* (1), 30−37.
(39) Hammouda, B. A new Guinier−Porod model. *J. Appl. Crystallogr.* **2010**, *43* (4), 716−719.
(40) Ilavsky, J.; Jemian, P. R. Irena: tool suite for modeling and analysis of small-angle scattering. *J. Appl. Crystallogr.* **2009**, *42* (2), 347−353.
(41) Guan, L.-Z.; Gong, L.-X.; Tang, L.-C.; Wu, L.-B.; Jiang, J.-X.; Lai, G.-Q. Mechanical properties and fracture behaviors of epoxy composites with phase-separation formed liquid rubber and preformed powdered rubber nanoparticles: A comparative study. *Polym. Compos.* **2015**, *36* (5), 785−799.
(42) Constable, G. S.; Lesser, A. J.; Coughlin, E. B. Morphological and Mechanical Evaluation of Hybrid Organic−Inorganic Thermoset Copolymers of Dicyclopentadiene and Mono- or Tris(norbornenyl)-Substituted Polyhedral Oligomeric Silsesquioxanes. *Macromolecules* **2004**, *37* (4), 1276−1282.
(43) Li, H.; Wang, Z.; Wang, Y.; He, B. Ring-opening metathesis polymerization of dicyclopentadiene catalyzed by a polymer-supported tungsten catalyst. *React. Funct. Polym.* **1997**, *33* (2−3), 193−200.
(44) Yang, G.; Lee, J. K. Curing Kinetics and Mechanical Properties of endo-Dicyclopentadiene Synthesized Using Different Grubbs' Catalysts. *Ind. Eng. Chem. Res.* **2014**, *53* (8), 3001−3011.
(45) Kirk-Othmer Encyclopedia of Chemical Technology.
(46) Jeong, W.; Kessler, M. R. Toughness Enhancement in ROMP Functionalized Carbon Nanotube/Polydicyclopentadiene Composites. *Chem. Mater.* **2008**, *20* (22), 7060−7068.
(47) Kleiner, L. W.; Karasz, F. E.; MacKnight, W. J. Compatible glassy polyblends based upon poly(2,6-dimethyl-1,4-phenylene oxide): Tensile modulus studies. *Polym. Eng. Sci.* **1979**, *19* (7), 519−524.
(48) Hayes, M. D.; Edwards, D. B.; Shah, A. R. 4 - Fractography Basics. In *Fractography in Failure Analysis of Polymers*; William Andrew Publishing: Oxford, 2015; pp 48−92.
(49) Beaumont, P.; Young, R. Failure of Brittle Polymers by Slow Crack Growth 0.1. Crack-Propagation. *J. Mater. Sci.* **1975**, *10* (8), 1334−1342.
(50) Young, R.; Beaumont, P. Failure of Brittle Polymers by Slow Crack Growth 0.2. Failure Processes. *J. Mater. Sci.* **1975**, *10* (8), 1343−1350.
(51) Young, R.; Beaumont, P. Failure of Brittle Polymers by Slow Crack Growth 0.3. Effect of Composition Upon Fracture of Silica Particle-Filled Epoxy-Resin Composites. *J. Mater. Sci.* **1977**, *12* (4), 684−692.
(52) Plangsangmas, L.; Mecholsky, J. J.; Brennan, A. B. Determination of fracture toughness of epoxy using fractography. *J. Appl. Polym. Sci.* **1999**, *72* (2), 257−268.
(53) Wenbo, L.; Tingqing, Y. Computer simulation of conic-shaped patterns on fracture surfaces of polymers. *J. Appl. Polym. Sci.* **2003**, *89* (6), 1722−1725.
(54) Fracture Appearance and Mechanisms of Deformation and Fracture - Heat Treating Society.
(55) Standard Practice for Interpreting Glass Fracture Surface Features, ASTM International, 2013.
(56) Standard Practice for Fractographic Analysis of Fracture Mirror Sizes in Ceramics and Glasses, ASTM International, 2015.
(57) Dear, D. J. P. A study of polymer fracture surface features and their relationship to toughness. *J. Mater. Sci.* **1999**, *34* (20), 4897−4907.
(58) Jin, H.; Miller, G. M.; Sottos, N. R.; White, S. R. Fracture and fatigue response of a self-healing epoxy adhesive. *Polymer* **2011**, *52* (7), 1628−1634.
(59) Zeman, J. Micromechanical Analysis of Composites.
(60) Guerra, C.; Scheibert, J.; Bonamy, D.; Dalmas, D. Understanding fast macroscale fracture from microcrack post mortem patterns. *Proc. Natl. Acad. Sci. U. S. A.* **2012**, *109* (2), 390−394.
(61) Landis, C. M.; Pardoen, T.; Hutchinson, J. W. Crack velocity dependent toughness in rate dependent materials. *Mech. Mater.* **2000**, *32* (11), 663−678.
(62) Sue, H. J.; Meitin, E. I. G.; Pickelman, D. M.; Bott, C. J. Fracture Mechanisms in Rigid Core-shell Particle Modified High Performance Epoxies. *Colloid Polym. Sci.* **1996**, *274* (4), 342−349.

DOI: 10.1021/acs.macromol.6b01649
Macromolecules XXXX, XXX, XXX−XXX

(63) Liang, Y. L.; Pearson, R. A. Toughening mechanisms in epoxy−silica nanocomposites (ESNs). *Polymer* **2009**, *50* (20), 4895−4905.
(64) Deblieck, R. A. C.; van Beek, D. J. M.; Remerie, K.; Ward, I. M. Failure mechanisms in polyolefines: The role of crazing, shear yielding and the entanglement network. *Polymer* **2011**, *52* (14), 2979−2990.
(65) Ritchie, R. O. The conflicts between strength and toughness. *Nat. Mater.* **2011**, *10* (11), 817−822.
(66) Quinn, G. D. *NIST Recommended Practice Guide Fractography of Ceramics and Glasses*; NIST SP 960-16e2; National Institute of Standards and Technology: 2016.

DOI: 10.1021/acs.macromol.6b01649
Macromolecules XXXX, XXX, XXX−XXX